

Simple Process-Led Algorithms for Simulating Habitats (SPLASH v.1.0): Robust Indices of Radiation, Evapotranspiration and Plant-Available Moisture

Tyler W. Davis^{1,*}, I. Colin Prentice^{1,2,3,4}, Benjamin D. Stocker¹, Rebecca T. Thomas¹, Rhys J. Whitley^{2,4}, Han Wang^{2,3}, Bradley J. Evans^{4,5}, Angela V. Gallego-Sala⁶, Martin T. Sykes⁷, and Wolfgang Cramer⁸

¹AXA Chair of Biosphere and Climate Impacts, Grand Challenges in Ecosystems and the Environment and Grantham Institute - Climate Change and the Environment, Department of Life Sciences, Imperial College London, Silwood Park Campus, Ascot, United Kingdom

²Department of Biological Sciences, Macquarie University, North Ryde, New South Wales, Australia

³State Key Laboratory of Soil Erosion and Dryland Farming on the Loess Plateau, College of Forestry, Northwest Agriculture & Forestry University, Yangling 712100, China

⁴Terrestrial Ecosystem Research Network (TERN) Ecosystem Modelling and Scaling Infrastructure (eMAST), Sydney, New South Wales, Australia

⁵Faculty of Agriculture and Environment, Department of Environmental Sciences, The University of Sydney, Sydney, New South Wales, Australia

⁶Department of Geography, University of Exeter, Exeter, Devon, United Kingdom

⁷Department of Physical Geography and Ecosystem Science, Lund University, Lund, Sweden

⁸Mediterranean Institute of marine and terrestrial Biodiversity and Ecology (IMBE), Aix Marseille University, CNRS, IRD, Avignon University, Aix-en-Provence, France

*now at: United States Department of Agriculture-Agricultural Research Service, Robert W. Holley Center for Agriculture and Health, Ithaca, United States

Correspondence to: I. Colin Prentice (c.prentice@imperial.ac.uk)

Abstract. Bioclimatic indices for use in studies of ecosystem function, species distribution, and vegetation dynamics under changing climate scenarios depend on estimates of surface fluxes and other quantities, such as radiation, evapotranspiration and soil moisture, for which direct observations are sparse. These quantities can be derived indirectly from meteorological variables, such as near-surface air temperature, precipitation and cloudiness. Here we present a consolidated set of Simple Process-Led Algorithms for Simulating Habitats (SPLASH) allowing robust approximations of key quantities at ecologically relevant time scales. We specify equations, derivations, simplifications and assumptions for the estimation of daily and monthly quantities of top-of-the-atmosphere solar radiation, net surface radiation, photosynthetic photon flux density, evapotranspiration (potential, equilibrium and actual), condensation, soil moisture, and runoff, based on analysis of their relationship to fundamental climatic drivers. The climatic drivers include a minimum of three meteorological inputs: precipitation, air temperature, and fraction of bright sunshine hours. Indices, such as the moisture index, the climatic water deficit, and the Priestley-Taylor coefficient, are also defined. The SPLASH code is transcribed in C++, FORTRAN, Python, and R. One year of results are presented at the local and global scales to exemplify the spatiotemporal patterns of daily and monthly model outputs along with comparisons to other model results.

1 Introduction

Despite the existence of dense networks of meteorological monitoring stations around the world, plant ecophysiology and biogeography suffer from a lack of globally distributed observational data, especially those central to the estimation of ecosystem-level photosynthesis, including photosynthetic photon flux density and soil moisture. To overcome this deficiency, we present
5 Simple Process-Led Algorithms for Simulating Habitats (SPLASH) for generating driving datasets for ecological and land-surface models (e.g., monthly carbon and water fluxes or seasonal plant functional trait distributions) from more readily available meteorological observations.

SPLASH is a continuation of the STASH (STatic SHell) model, which was originally developed for modeling the climatic controls on plant species distributions at a regional scale (Sykes and Prentice, 1995, 1996; Sykes et al., 1996). The intention of STASH was to provide bioclimatic indices, reflecting the environment experienced by plants more closely than either
10 standard summary variables such as mean annual temperature, or such constructions as ‘mean precipitation of the warmest quarter,’ while requiring only standard meteorological data as input. A key component of STASH was a simple, physically-based soil moisture accounting scheme, first developed by Cramer and Prentice (1988), which has been used *inter alia* in the original, highly cited BIOME model (Prentice et al., 1992); the general forest succession model (FORSKA) described by
15 Prentice et al. (1993); and the Simple Diagnostic Biosphere Model (Knorr and Heimann, 1995). Despite the subsequent development of more complex Dynamic Global Vegetation Models (Cramer et al., 2001; Sitch et al., 2003; Woodward and Lomas, 2004; Quillet et al., 2010; Prentice and Cowling, 2013; Fisher et al., 2014) and Land Surface Models, the relatively simple algorithms in STASH continue to have many applications, including to new areas such as the distribution of plant functional traits (Harrison et al., 2010; Meng et al., 2015), assessment of climate-change impacts on specific biomes (Gallego-Sala and Prentice,
20 2012), large-scale water resources assessments (e.g. Ukkola et al., 2015) and simple first-principles modeling of primary production (Wang et al., 2014). The continuing utility of these algorithms owes much to their robustness, which in turn depends on the implicit assumption that vegetation functions predictably—so that, for example, evapotranspiration occurs at a potential rate under well-watered conditions, and is reduced as soil water is drawn down. STASH is thus unsuitable to answer questions like the effect of imposed vegetation changes on runoff, or modeling vegetation-atmosphere feedbacks. Much more complex
25 models that dynamically couple soil, vegetation and atmospheric boundary layer processes exist for such applications; however, their complexity brings a burden in terms of lack of robustness and, potentially, large inter-model differences (Prentice et al., 2014).

Despite their long history of use, no single publication documents the algorithms of the STASH model. This work aims to fill that gap to allow for the continued development and use of these algorithms. As the new incarnation of STASH, SPLASH
30 provides the same physically-based soil moisture accounting scheme with updated and corrected analytical expressions for the calculation of daily radiation, evapotranspiration, and soil moisture. Included in this documentation are the equation derivations, variable definitions, and information regarding model assumptions and limitations. One notable improvement is that we have discontinued the approximation of constant angular velocity in the orbit of Earth around the Sun. This version is thus suitable

for palaeoclimate applications, whereby orbital precession (as well as changes in obliquity and eccentricity) influences the seasonal distribution of insolation. SPLASH also includes explicit consideration of elevation effects on biophysical quantities.

Key model outputs include daily insolation (incoming solar radiation at the top of the atmosphere) and net surface radiation (H_o and H_N , respectively); daily photosynthetic photon flux density (Q_n); daily condensation, soil moisture and runoff (C_n , W_n , and RO); and daily equilibrium, potential and actual evapotranspiration (E_n^q , E_n^p , and E_n^a). Unlike the STASH model, SPLASH explicitly distinguishes potential and equilibrium evapotranspiration, recognizing that under well-watered conditions the excess of the former over the latter is a requirement for foliage to be cooler than the surrounding air, as has long been observed under high environmental temperatures (e.g. Linacre, 1967).

Input values of latitude, ϕ (rad), elevation, z (m), mean daily near-surface air temperature, T_{air} ($^{\circ}\text{C}$), and fractional hours of bright sunshine, S_f (unitless), are used for calculating the daily quantities of net radiation and evapotranspiration. Daily precipitation, P_n (mm d^{-1}), is used for updating daily soil moisture. T_{air} and P_n may be derived from various sources, including the freely available daily-averaged air temperature and precipitation reanalysis data from the Water and Global Change (WATCH) program’s meteorological forcing data set (Weedon et al., 2014). Meteorological variables are also available in the Climatic Research Unit (CRU) gridded monthly time series datasets (Harris et al., 2014), which may be downscaled to daily quantities by means of quasi-daily methods (e.g., linear interpolation). Cloud cover fraction, for example the simulated quantities given in the CRU TS3.21 dataset, may be used to approximate S_f . Penman’s one-complement approximation based on the cloudiness fraction is regarded here as a sufficient estimate of S_f (Penman, 1948). The piecewise linear method of Hulme et al. (1995)—an adaptation of the Doorenbos-Pruitt estimation procedure (Doorenbos and Pruitt, 1977)—as used in the development of the CRU cloudiness climatology (New et al., 1999) gives similar results.

We present SPLASH comprehensively re-coded in a modular framework to be readable, understandable and reproducible. To facilitate varied application requirements (including computational speed), four versions of the code (C++, FORTRAN, Python, and R) are available in an online repository (see Code Availability). The algorithms as presented here focus on application to individual site locations, but a natural extension is towards spatially distributed grid-based datasets.

In line with the intention of the original STASH algorithms, we also present bioclimatic indices at the monthly and annual timescales to exemplify the analytical applications of the SPLASH model outputs.

2 Methodology

The implementation of the soil-moisture accounting scheme follows the steps outlined by Cramer and Prentice (1988), where daily soil moisture, W_n (mm), is calculated based on the previous day’s moisture content, W_{n-1} , incremented by daily precipitation, P_n (mm d^{-1}), and condensation, C_n (mm d^{-1}), and reduced by daily actual evapotranspiration, E_n^a (mm d^{-1}) and runoff, RO (mm):

$$W_n = W_{n-1} + P_n + C_n - E_n^a - RO, \quad (1)$$

where P_n is a model input, C_n is estimated based on the daily negative net radiation, E_n^a is the analytical integral of the minimum of the instantaneous evaporative supply and demand rates over a single day, and RO is the amount of soil moisture

in excess of the holding capacity. An initial condition of W_n is assumed between zero and the maximum soil moisture capacity, W_m (mm), for a given location and is equilibrated over an entire year by successive model iterations (i.e., model spin-up). Under steady-state conditions, the SPLASH model preserves the water balance, such that $\sum (P_n + C_n) = \sum (E_n^a + RO)$.

To solve the simple ‘bucket model’ represented by Eq. 1, the following steps are taken at the daily timescale: calculate the radiation terms, estimate the condensation, estimate the evaporative supply, estimate the evaporative demand, calculate the actual evapotranspiration, and update the daily soil moisture. Daily quantities may be aggregated into monthly and annual totals and used in moisture index calculations.

2.1 Radiation

2.1.1 Top-of-the-atmosphere solar radiation

The calculation of C_n and E_n^a begin with modeling the extraterrestrial solar radiation flux, I_o (W m^{-2}). The equation for I_o may be expressed as the product of three terms (Duffie and Beckman, 2013):

$$I_o = I_{sc} d_r \cos \theta_z, \quad (2)$$

where I_{sc} (W m^{-2}) is the solar constant, d_r (unitless) is the distance factor, and $\cos \theta_z$ (unitless) is the inclination factor. Values for I_{sc} may be found in the literature (e.g., Thekaekara and Drummond, 1971; Willson, 1997; Dewitte et al., 2004; Fröhlich, 2006; Kopp and Lean, 2011); a constant for I_{sc} is given in Table 2.

The distance factor, d_r , accounts for additional variability in I_o that reaches the Earth. This variability is due to the relative change in distance between Earth and the Sun caused by the eccentricity of Earth’s elliptical orbit, e (unitless), and is calculated as (Berger et al., 1993):

$$d_r = \left(\frac{1 + e \cos \nu}{1 - e^2} \right)^2, \quad (3)$$

where ν (rad) is Earth’s true anomaly. True anomaly is the measure of Earth’s location around the Sun relative to its position when it is closest to the Sun (perihelion).

The last term, $\cos \theta_z$, attenuates I_o to account for the Sun’s height above the horizon (measured relative to the zenith angle, θ_z), accounting for the off-vertical tilt of Earth’s rotational axis, ε (i.e., obliquity). The inclination factor is calculated as (Duffie and Beckman, 2013):

$$\cos \theta_z = \sin \delta \sin \phi + \cos \delta \cos \phi \cos h, \quad (4)$$

where ϕ (rad) is the latitude, δ (rad) is the declination angle, and h (rad) is the hour angle, measuring the angular displacement of the Sun east or west of solar noon ($-\pi \leq h \leq \pi$). Declination is the angle between Earth’s equator and the Sun at solar noon ($h = 0$), varying from $+\varepsilon$ at the June solstice to $-\varepsilon$ at the December solstice; the changing declination is responsible for the change in seasons. For the purposes of ecological modeling, δ may be assumed constant throughout a single day. See e.g.

Woolf (1968) for the precise geometric equation representing δ :

$$\delta = \arcsin(\sin \lambda \sin \varepsilon), \quad (5)$$

where λ (rad) is Earth's true longitude (i.e., the heliocentric longitude relative to Earth's position at the vernal equinox) and ε (rad) is obliquity (i.e., the slowly varying tilt of Earth's axis). Several other methods are widely used for the estimation of δ for a given day of the year (e.g., Cooper, 1969; Spencer, 1971; Swift, 1976) but are not recommended because they do not account for the change in Earth's orbital velocity with respect to the distance between Earth and the Sun, while Eq. 5 does. The relationship between true longitude, λ , and true anomaly, ν , is by the angle of the perihelion with respect to the vernal equinox, $\tilde{\omega}$ (rad) (Berger, 1978):

$$\nu = \lambda - \tilde{\omega}. \quad (6)$$

While the three orbital parameters (i.e., e , ε , and $\tilde{\omega}$) exhibit long-term variability (on the order of tens of thousands of years), they may be treated as constants for a given epoch (e.g., $e = 0.0167$, $\varepsilon = 23.44^\circ$, and $\tilde{\omega} = 283.0^\circ$ for 2000 CE), or they may be calculated using the methods of Berger (1978) or Berger and Loutre (1991) for palaeoclimate studies. Berger (1978) presents a simple algorithm to estimate λ for a given day of the year (see Appendix A).

The daily top-of-the-atmosphere solar radiation, H_o (J m^{-2}), may be calculated as twice the integral of I_o measured between solar noon and the sunset angle, h_s , assuming that all angles related to Earth on its orbit are constant over a whole day:

$$H_o = \int_{\text{day}} I_o = 2 \int_{h=0}^{h_s} I_o = \frac{86400}{\pi} I_{sc} d_r (r_u h_s + r_v \sin h_s), \quad (7)$$

where $r_u = (\sin \delta \sin \phi)$ and $r_v = (\cos \delta \cos \phi)$, both unitless.

The sunset angle can be calculated as the hour angle when the solar radiation flux reaches the horizon (i.e., when $I_o = 0$) and can be found by substituting Eq. 4 into Eq. 2, setting I_o equal to zero, and solving for h :

$$h_s = \arccos\left(-\frac{r_u}{r_v}\right). \quad (8)$$

To account for the undefined negative fluxes produced by Eq. 2 for $h \geq h_s$ and $h \leq -h_s$, I_o should be set equal to zero during these nighttime hours. To account for the occurrences of polar day (i.e., no sunset) and polar night (i.e., no sunrise), h_s should be limited to π when $r_u/r_v \geq 1$ and zero when $r_u/r_v \leq -1$.

2.1.2 Net surface radiation

The net surface radiation, H_N (J m^{-2}), is the integral of the net surface radiation flux received at the land surface, I_N (W m^{-2}), which is classically defined as the difference between the net incoming shortwave radiation flux, I_{SW} (W m^{-2}) and the net outgoing longwave radiation flux, I_{LW} (W m^{-2}):

$$I_N = I_{SW} - I_{LW}. \quad (9)$$

The calculation of I_{SW} is based on the reduction in I_o due to atmospheric transmittivity, τ (unitless), and surface shortwave albedo, β_{sw} (unitless):

$$I_{SW} = (1 - \beta_{sw}) \tau I_o. \quad (10)$$

A constant value for β_{sw} is given in Table 2. Atmospheric transmittivity may be expressed as a function of elevation (to account for attenuation caused by the mass of the atmosphere) and cloudiness (to account for atmospheric turbidity). At higher elevations, there is less atmosphere through which shortwave radiation must travel before reaching the surface. To account for this, Allen (1996) presents an equation based on the regression of Beer's radiation extinction function at elevations below 5 3000 m with an average sun angle of 45° , which can be expressed as:

$$\tau = \tau_o (1 + 2.67 \times 10^{-5} z), \quad (11)$$

where z (m) is the elevation above mean sea level and τ_o (unitless) is the mean sea-level transmittivity, which can be approximated by the Ångström-PreScott formula:

$$\tau_o = c + d S_f, \quad (12)$$

10 where c and d are empirical constants (unitless) and S_f is the fraction of daily bright sunshine hours ($0 \leq S_f \leq 1$). Values for c and d are given in Table 2.

The calculation of I_{LW} is based on the difference between outgoing and incoming longwave radiation fluxes attenuated by the presence of clouds, which may be empirically estimated by (Linacre, 1968):

$$I_{LW} = [b + (1 - b) S_f] (A - T_{air}), \quad (13)$$

15 where A and b are empirical constants and T_{air} ($^\circ\text{C}$) is the mean near-surface air temperature. The outgoing longwave radiation flux used to derive Eq. 13 assumes a constant ground emissivity, which is accurate under well-watered conditions. The incoming longwave radiation flux is modeled based on clear-sky formulae derived by Linacre (1968). Values for A and b are given in Table 2.

H_N can be decomposed into its net positive, H_N^+ (J m^{-2}), and net negative, H_N^- (J m^{-2}), components (i.e., $H_N = H_N^+ +$
20 H_N^-). Assuming I_{LW} is constant throughout the day and making substitutions for I_o into Eq. 10, an expression for H_N^+ may be derived as twice the integral of I_N between solar noon (i.e., $h = 0$) and the net surface radiation flux cross-over hour angle, h_n (rad):

$$H_N^+ = 2 \int_{h=0}^{h_n} I_N = \frac{86400}{\pi} [(r_w r_u - I_{LW}) h_n + r_w r_v \sin h_n], \quad (14)$$

where $r_w = (1 - \beta_{sw}) \tau I_{sc} d_r$ (W m^{-2}).

25 Here, h_n is the hour angle when I_{SW} equals I_{LW} and can be found by setting $I_N = 0$ in Eq. 9 and solving for h , following the same substitutions as used for h_s in Eq. 8, and may be expressed as:

$$h_n = \arccos\left(\frac{I_{LW} - r_w r_u}{r_w r_v}\right). \quad (15)$$

To account for the occurrences when the net surface radiation flux does not cross the zero datum, h_n should be limited to π when $(I_{LW} - r_w r_u)/(r_w r_v) \leq -1$ (i.e., net surface radiation flux is always positive) and zero when $(I_{LW} - r_w r_u)/(r_w r_v) \geq 1$
30 (i.e., net surface radiation flux is always negative).

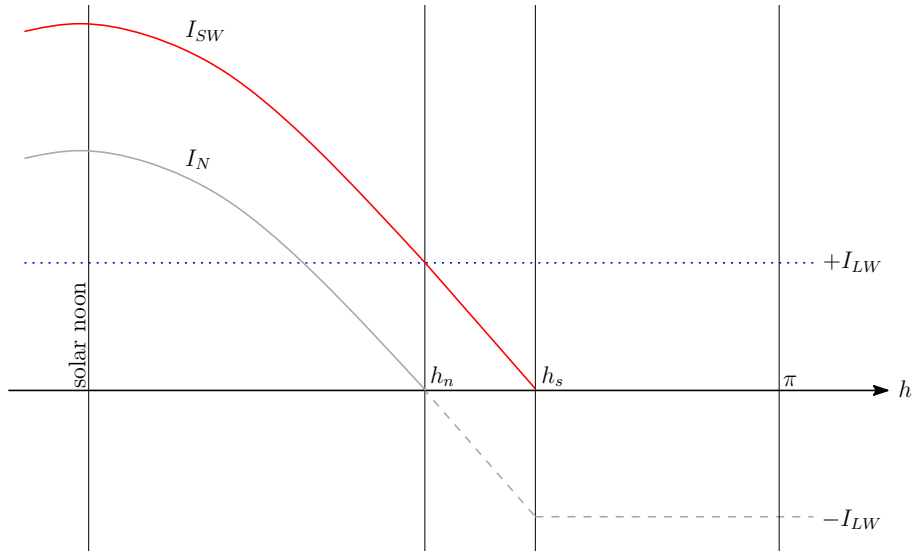


Figure 1. Example of the net radiation flux curve between the hours of solar noon (i.e., $h = 0$) and solar midnight (i.e., $h = \pi$). The I_N curve is equal to the difference between the net incoming shortwave radiation flux, I_{SW} (solid red line), and the net outgoing longwave radiation flux, I_{LW} (dotted blue line). Positive I_N , shown decreasing from solar noon to zero at the cross-over hour angle, h_n , is denoted with a solid gray line, while negative I_N , shown decreasing from zero to $-I_{LW}$ between h_n and the sunset hour angle, h_s , and constant between h_s and solar midnight, is denoted with a dashed gray line. The solid black horizontal line marks the datum of zero radiation.

Complementary to H_N^+ , H_N^- may be calculated as twice the integral of I_N between h_n and solar midnight, defined by the piecewise function of I_N between h_n and h_s and $-I_{LW}$ between h_s and solar midnight (i.e., $h = \pi$), given as (note that H_N^- is a negative quantity):

$$H_N^- = 2 \left(\int_{h_n}^{h_s} I_N - \int_{h_s}^{\pi} I_{LW} \right) = \frac{86400}{\pi} [r_w r_v (\sin h_s - \sin h_n) + r_w r_u (h_s - h_n) - I_{LW} (\pi - h_n)]. \quad (16)$$

- 5 Figure 1 shows an example of a half-day I_N curve used in the integrals defined in Eqns. 14 and 16. I_N , which is at its peak at solar noon, crosses zero at h_n and reaches a minimum at h_s . After sunset (i.e., $h > h_s$), when I_{SW} is zero, I_N is equal to $-I_{LW}$. H_N^+ is represented as twice the integral under the positive net radiation curve (solid gray line), above the zero line (solid black line), and between the vertical lines of solar noon and h_n . H_N^- is represented as twice the integral below the zero line and above the negative net radiation curve (dashed gray line).

10 2.1.3 Photosynthetically active radiation

The daily photosynthetically active radiation in units of photon flux density, Q_n ($\text{mol m}^{-2} \text{d}^{-1}$), is calculated based on the number of quanta received (moles of photons) within the visible light spectrum, which also corresponds to the action spectrum

of photosynthesis (Monteith and Unsworth, 1990):

$$Q_n = 1 \times 10^{-6} \text{ fFEC } (1 - \beta_{vis}) \tau H_o, \quad (17)$$

where β_{vis} (unitless) is the visible light albedo and fFEC ($\mu\text{mol J}^{-1}$) is the flux-to-energy conversion factor (Ge et al., 2011). This factor takes into account both the portion of visible light within the total solar spectrum, approximately 50% (Stanhill and Fuchs, 1977), and the mean number of quanta in the visible light energy band, approximately $4.6 \mu\text{mol J}^{-1}$ (McCree, 1972). The 1×10^{-6} converts the units of Q_n from $\mu\text{mol m}^{-2} \text{d}^{-1}$ to $\text{mol m}^{-2} \text{d}^{-1}$. Values for β_{vis} and fFEC are given in Table 2.

2.2 Condensation

The daily condensation, C_n , may be expressed as the water-equivalent of the absolute value of negative net radiation, H_N^- :

$$C_n = 1 \times 10^3 E_{con} |H_N^-|, \quad (18)$$

where E_{con} ($\text{m}^3 \text{J}^{-1}$) is the water-to-energy conversion factor that relates the energy released or required for a unit volume of water to evaporate or condense at a given temperature and pressure, which may be expressed as:

$$E_{con} = \frac{s}{L_v \rho_w (s + \gamma)}, \quad (19)$$

where s (Pa K^{-1}) is the slope of the saturation vapor pressure-temperature curve, L_v (J kg^{-1}) is the latent heat of vaporization of water, ρ_w (kg m^{-3}) is the density of water, and γ (Pa K^{-1}) is the psychrometric constant. Standard values may be assumed for certain parameters (e.g., $L_v = 2.5 \times 10^6 \text{ J kg}^{-1}$; $\rho_w = 1 \times 10^3 \text{ kg m}^{-3}$; $\gamma = 65 \text{ Pa K}^{-1}$); however, equations for the temperature dependence of s and L_v (e.g., Allen et al., 1998; Henderson-Sellers, 1984) and the temperature and pressure dependence of ρ_w and γ (e.g., Kell, 1975; Chen et al., 1977; Allen et al., 1998; Tsilingiris, 2008) are available (see Appendix B).

The barometric formula may be used to estimate the atmospheric pressure, P_{atm} (Pa), at a given elevation, z (m), when observations are not available. Assuming a linear decrease in temperature with height, which is a reasonable approximation within the troposphere (i.e., for $z < 1.10 \times 10^4 \text{ m}$), the following equation may be used (Berberan-Santos et al., 1997):

$$P_{atm} = P_o \left(1 - \frac{L z}{T_o} \right)^{\frac{g M_a}{R L}}, \quad (20)$$

where P_o (Pa) is the base pressure, T_o (K) is the base temperature, z (m) is the elevation above mean sea level, L (K m^{-1}) is the mean adiabatic lapse rate of the troposphere, g (m s^{-2}) is the standard gravity, M_a (kg mol^{-1}) is the molecular weight of dry air, and R ($\text{J mol}^{-1} \text{K}^{-1}$) is the universal gas constant. Values for the constants used in Eq. 20 are given in Table 2.

2.3 Evaporative Supply

The evaporative supply rate, S_w (mm h^{-1}) is assumed to be constant over the day and can be estimated based on a linear proportion of the previous day's soil moisture, W_{n-1} (Federer, 1982):

$$S_w = S_c \frac{W_{n-1}}{W_m}, \quad (21)$$

where S_c (mm h^{-1}) is the supply rate constant (i.e., maximum rate of evaporation) and W_m (mm) is the maximum soil moisture capacity. Constant values for S_c and W_m are given in Table 2.

2.4 Evaporative Demand

The evaporative demand rate, D_p (mm h^{-1}), is set equal to the potential evapotranspiration rate, E^p (mm h^{-1}), as defined by Priestley and Taylor (1972). E^p usually exceeds the equilibrium evapotranspiration rate, E^q (mm h^{-1}), due to the entrainment of dry air in the convective boundary layer above an evaporating surface (Raupach, 2000, 2001). E^p is related to E^q by the Priestley-Taylor coefficient, which may be defined as one plus an entrainment factor, ω (Lhomme, 1997):

$$D_p = E^p = (1 + \omega) E^q. \quad (22)$$

The constant value used for ω is given in Table 2. The calculation of E^q is based on the energy-water equivalence of I_N , ignoring the soil heat flux, (Lhomme, 1997):

$$E^q = 3.6 \times 10^6 E_{con} I_N, \quad (23)$$

where 3.6×10^6 converts the units of E^q from m s^{-1} to mm h^{-1} . Note that E^q is defined only for positive values (i.e., $E^q = 0$ for $I_N < 0$). The Priestley-Taylor potential evapotranspiration is preferred in this context to the general Penman-Monteith equation for actual evapotranspiration (Penman, 1948; Monteith, 1965), which requires knowledge of stomatal and aerodynamic conductances, or to any of the ‘reference evapotranspiration’ formulae (Allen et al., 1998) that specifically relate to agricultural crops.

Daily equilibrium evapotranspiration, E_n^q (mm d^{-1}), is based on the integration of Eq. 23 for values of positive I_N , or simply the energy-water equivalence of H_N^+ :

$$E_n^q = 1 \times 10^3 E_{con} H_N^+, \quad (24)$$

where 1×10^3 converts E_n^q from m d^{-1} to mm d^{-1} .

The daily demand, which is equal to the daily potential evapotranspiration, E_n^p (mm d^{-1}), may be calculated from E_n^q , as in Eq. 22:

$$E_n^p = (1 + \omega) E_n^q. \quad (25)$$

2.5 Actual Evapotranspiration

The calculation of daily actual evapotranspiration, E_n^a (mm d^{-1}), is based on the daily integration of the actual evapotranspiration rate, E^a (mm h^{-1}), which may be defined as the minimum of the evaporative supply and demand rates (Federer, 1982):

$$E^a = \min(S_w, D_p), \quad (26)$$

where S_w (mm h^{-1}) is the evaporative supply rate, defined in Eq. 21, and D_p (mm h^{-1}) is the evaporative demand rate, defined in Eq. 22.

The analytical solution to E_n^a may be expressed analogous to the methodology used for solving H_o and H_N and is defined as twice the integral of E^a between solar noon and h_n , which comprises two curves: S_w for $0 \leq h \leq h_i$ and D_p for $h_i \leq h \leq h_n$, where h_i (rad) is the hour angle corresponding to the intersection of S_w and D_p (i.e., when $S_w = D_p$):

$$E_n^a = 2 \int_{h=0}^{h_n} E^a = 2 \left(\int_0^{h_i} S_w + \int_{h_i}^{h_n} D_p \right), \quad (27a)$$

5 which may be expressed as:

$$E_n^a = \frac{24}{\pi} [S_w h_i + r_x r_w r_v (\sin h_n - \sin h_i) + (r_x r_w r_u - r_x I_{LW}) (h_n - h_i)], \quad (27b)$$

where $r_x = 3.6 \times 10^6 (1 + \omega) E_{con}$ ($\text{mm m}^2 \text{W}^{-1} \text{h}^{-1}$). The intersection hour angle, h_i , is defined by setting Eq. 21 equal to Eq. 22 and solving for h :

$$h_i = \arccos \left(\frac{S_w}{r_x r_w r_v} + \frac{I_{LW}}{r_w r_v} - \frac{r_u}{r_v} \right). \quad (28)$$

10 To account for the occurrences when supply is in excess of demand during the entire day, h_i should be limited to zero when $\cos h_i \geq 1$. For occurrences when supply limits demand during the entire day, h_i should be limited to π when $\cos h_i \leq -1$.

Figure 2 shows an example of the half-day evaporative supply and demand rate curves. D_p (dashed red line) is at a maximum at solar noon and decreases down to zero at h_n , while S_w (dotted blue line) is constant throughout the day. The point where S_w equals D_p is denoted by the vertical bar at h_i . E^a (solid gray line), limited by supply during most of the day, follows the S_w line between solar noon and h_i . During the time between h_i and h_n , E^a no longer limited by supply, follows the D_p curve. After h_n , both D_p and E^a are zero. E_n^a is represented by twice the area above the zero line (horizontal solid black line), below the E^a line, and between the vertical bars of solar noon and h_n .

2.6 Runoff

The calculation of daily runoff, RO , is based on the excess of daily soil moisture without runoff compared to the holding capacity, W_m , and is given by:

$$RO = \max(0, W_n^* - W_m), \quad (29)$$

where W_n^* (mm) is the daily soil moisture without runoff (i.e., Eq. 1 where $RO = 0$).

2.7 Soil Moisture

With analytical expressions for C_n , E_n^a and RO (i.e., Eqns. 18, 27b and 29, respectively), W_n may now be calculated by Eq. 1. Once W_n is calculated, the following limits are checked:

$$0 \leq W_n \leq W_m. \quad (30)$$

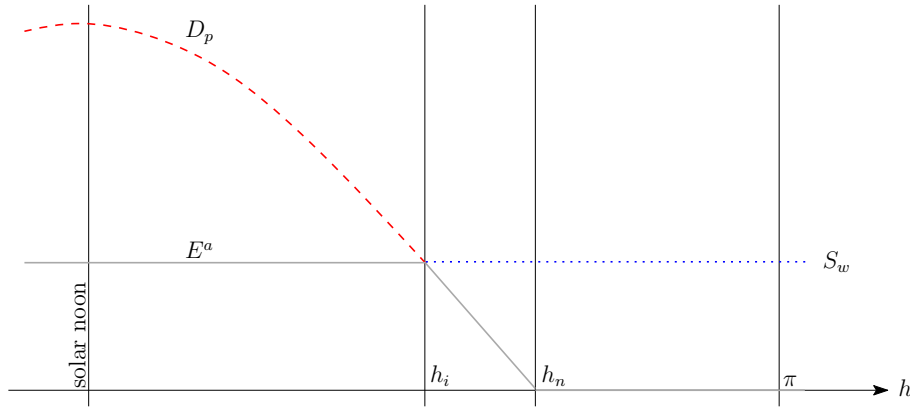


Figure 2. Example of actual evapotranspiration curve between the hours of solar noon (i.e., $h = 0$) and solar midnight (i.e. $h = \pi$). The evaporative demand, D_p (dashed red line), is at a maximum at solar noon and zero at the cross-over hour angle, h_n . The evaporative supply, S_w (dotted blue line), is constant throughout the day. The point where supply is equal to demand denotes the intersection hour angle, h_i . Actual evapotranspiration (solid gray line) is defined as the minimum of S_w and D_p throughout the day.

The calculation of RO in Eq. 29 should prevent W_n from being greater than W_m , thus satisfying the upper limit of Eq. 30. The limiting effect of S_w on E_n^a , through Eqns. 27 and 28, should, in most cases, prevent W_n from falling below zero and satisfy the lower limit of Eq. 30; however, due to the assumption that S_w is constant throughout the day, there is the possibility that $E_n^a + RO$ may exceed $W_{n-1} + P_n + C_n$, resulting in negative W_n . In these rare cases, in order to maintain the mass balance of the bucket model presented in Eq. 1, E_n^a is reduced by an amount equal to the magnitude of the negative soil moisture.

3 Bioclimatic Indices

One application of the SPLASH model is estimating the surface fluxes required for the calculation of bioclimatic indices. Typically described at longer time scales (e.g., monthly or annually), the daily SPLASH fluxes can be integrated to monthly and annual totals:

$$10 \quad X_{m,a} = \sum_{d=1}^{N_{m,a}} X_d, \quad (31)$$

where X is a model output parameter at a given day (X_d), month (X_m), or year (X_a) and N is the total number of days to sum over for a given month (N_m) or a given year (N_a).

The following sections describe three common bioclimatic indices.

3.1 Moisture Index

15 There exists a long history that includes several variants of the moisture index, MI , also commonly referred to as the aridity index, AI , or moisture ratio, MR (Thornthwaite, 1948; Budyko, 1961). A current definition describes MI as the ratio of annual

precipitation to annual potential evapotranspiration (Middleton and Thomas, 1997), given as:

$$MI = \frac{P_a}{E_a^p}, \quad (32)$$

where P_a (mm a^{-1}) is the annual precipitation and E_a^p (mm a^{-1}) is the annual potential evapotranspiration as calculated by Eq. 31; P_a and E_a^p may be substituted with their multi-year means (i.e., \bar{P}_a and \bar{E}_a^p) if available. Values less than one are indicative of annual moisture deficit.

3.2 Climatic Water Deficit

The climatic water deficit, ΔE , defined as the difference between the evaporative demand (i.e., potential evapotranspiration) and the actual evapotranspiration, has been shown to be a biologically meaningful measure of climate as it pertains to both the magnitude and length of drought stress experienced by plants (Stephenson, 1998). At the monthly timescale, this index is calculated as:

$$\Delta E_m = E_m^p - E_m^a, \quad (33)$$

where ΔE_m (mm mo^{-1}) is the monthly climatic water deficit, E_m^p (mm mo^{-1}) is the monthly potential evapotranspiration and E_m^a (mm mo^{-1}) is the monthly actual evapotranspiration. E_m^p and E_m^a are the monthly totals of E_n^p and E_n^a , respectively, calculated by Eq. 31. Values of ΔE may also be computed at the annual timescale.

3.3 Priestley-Taylor Coefficient

The Priestley-Taylor coefficient, α , is the ratio of actual evapotranspiration to equilibrium evapotranspiration, which represents the fraction of plant-available surface moisture (Priestley and Taylor, 1972; Sykes et al., 1996; Gallego-Sala et al., 2010). At the monthly timescale, this is defined as:

$$\alpha_m = \frac{E_m^a}{E_m^q}, \quad (34)$$

where α_m is the monthly Priestley-Taylor coefficient, E_m^a is the monthly actual evapotranspiration and E_m^q (mm mo^{-1}) is the monthly equilibrium evapotranspiration. Due to the entrainment factor, α_m may vary between zero (i.e., no moisture) and $1 + \omega$ (i.e., unlimited moisture). Values of α may also be computed at the annual timescale.

4 Results

The methodology described in Sect. 2 was translated into computer application code (C++, FORTRAN, Python and R). The following sections describe the year-long SPLASH simulation results (2000 CE) at the local and global scales along with comparisons with other model results.

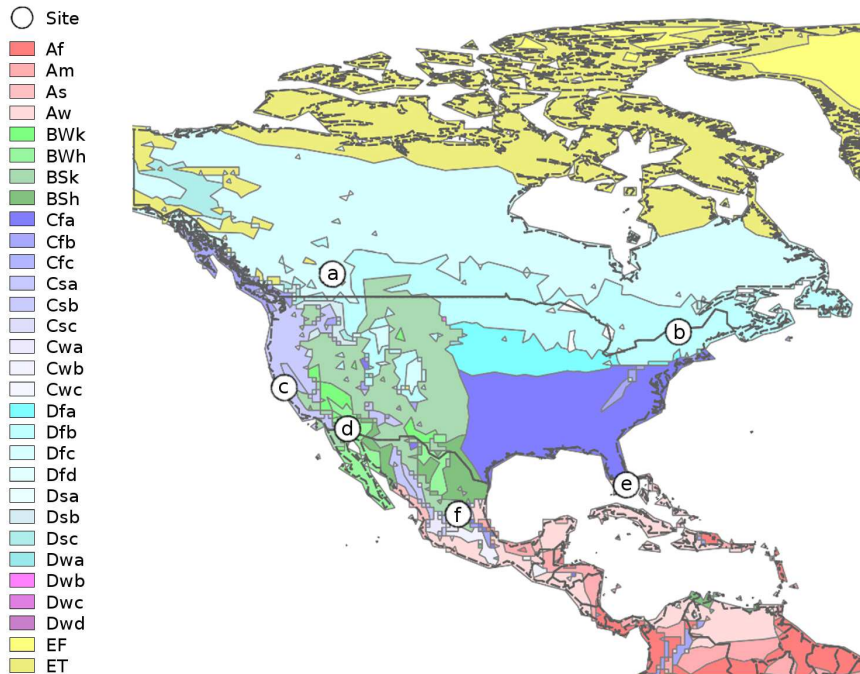


Figure 3. Map of Köppen-Geiger climate regions across North America (Kottek et al., 2006). Six locations are selected representing: (a) tundra—ET (51.8° N, 116.5° W, 1383 m.a.s.l.); (b) continental with warm summers—Dfb (44.7° N, 73.8° W, 383 m.a.s.l.); (c) temperate with dry summers—Csb (37.8° N, 122.4° W, 16 m.a.s.l.); (d) hot arid desert—BWh (32.7° N, 114.6° W, 43 m.a.s.l.); (e) equatorial monsoon—Am (26.0° N, 80.3° W, 2 m.a.s.l.); (f) cold arid steppe—BSk (22.2° N, 101.0° W, 1850 m.a.s.l.).

4.1 Local Temporal Trends and Bioclimatic Indices

The SPLASH model was run at six locations across North America (see Fig. 3), representing six distinct climate regions across latitudinal and elevational gradients. Ten years (i.e., 1991–2000) of monthly CRU TS3.23 data (i.e., precipitation, air temperature, and cloudiness fraction) were extracted from the $0.5^{\circ} \times 0.5^{\circ}$ pixel located over each site. Air temperature and cloudiness fraction were assumed constant and monthly precipitation was divided equally across each day of the month. Fractional sunshine hours were calculated as the one-complement of the cloudiness fraction. Orbital parameters (for paleoclimatology studies) were assumed constant and calculated for the 2000 CE epoch based on the methods of Berger (1978). Model constants were assigned as per Table 2.

The first year of the simulation (i.e., 1991) was iterated (approximately twice) until the daily soil moisture, initialized at zero, reached equilibrium, after which the model was spun-up for eight years (i.e., 1992–1999). The results, shown in Figs. 4 and 5, are for the year 2000. Accompanying the daily SPLASH results in Fig. 4, shown in red, are daily surface fluxes based on the three-layer Variable Infiltration Capacity (VIC) model, extracted from the $1/16^{\circ}$ pixel over each of the six sites from the datasets provided by Livneh et al. (2015).

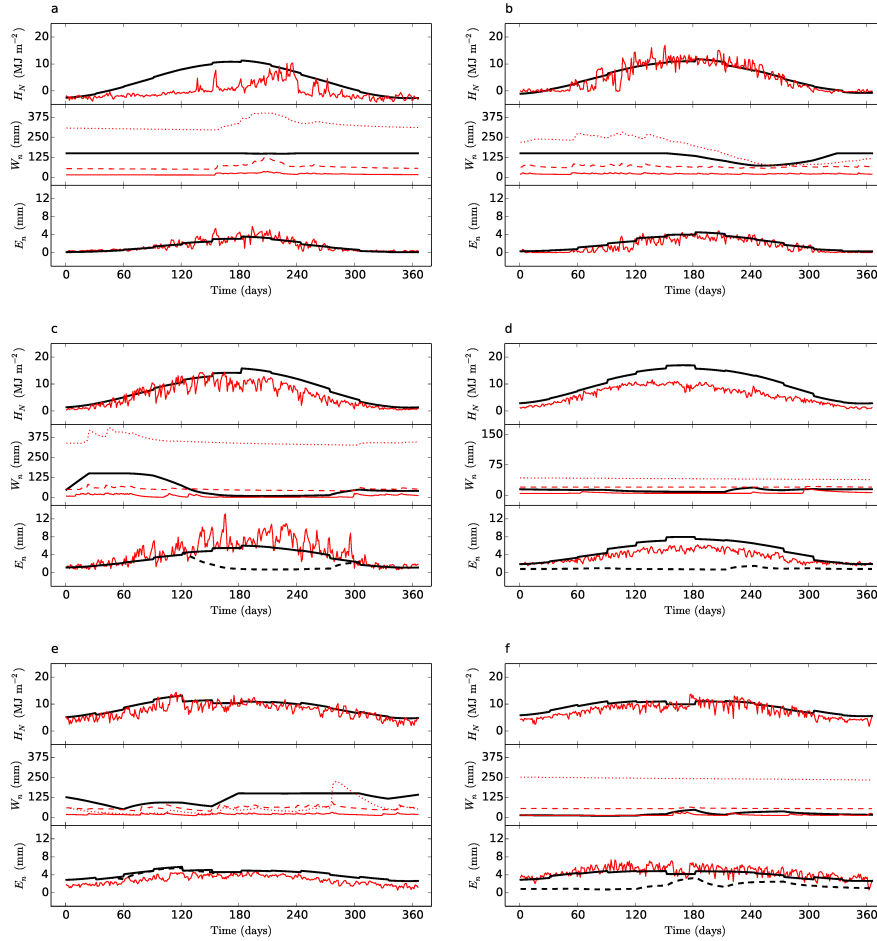


Figure 4. Daily simulations of net radiation, H_N , soil moisture, W_n , and evapotranspiration, E_n for the six climate regions defined in Fig. 3: (a) tundra, (b) continental with warm summers, (c) temperate with dry summers, (d) hot arid desert, (e) equatorial monsoon, and (f) cold arid steppe. Black lines represent SPLASH modeled net radiation, soil moisture, and evapotranspiration (potential in solid black and actual in dashed black). Red lines represent VIC three-layer modeled surface fluxes from Livneh et al. (2015) for net radiation, soil moisture (layer 1 in solid red, layer 2 in dashed red, and layer 3 in dotted red), and potential evapotranspiration. Days of the year are represented along the x-axis. Data are for one year (2000 CE).

Figure 4a shows the daily results for a tundra region over Banff National Park in Alberta, Canada with a mean annual temperature of $-4\text{ }^\circ\text{C}$ and annual precipitation of 986 mm. The SPLASH H_N depicts a bell-shaped curve characteristic for the northern hemisphere. During the spring and summer months, SPLASH H_N is higher than the VIC results, which exhibit a lower H_N during the first half of the year. The SPLASH W_n remains saturated throughout the year at a level between the second and third layers of VIC. SPLASH and VIC E_n^p are similar in magnitude throughout the year with SPLASH E_n^a following E_n^p all year.

Figure 4b shows the daily results for a continental warm summer region over the Adirondack region of New York with a mean annual temperature of 5 °C and annual precipitation of 1080 mm. There is agreement between the SPLASH and VIC H_N and E_n^p throughout the year. The SPLASH W_n remains saturated throughout most of the year with a dry-down period during mid to late summer and a recovery period during the autumn.

5 Figure 4c shows the daily results for a temperate region with dry summers over the Bay Area of California with a mean annual temperature of 14 °C and annual precipitation of 594 mm. During the dry summer months, SPLASH H_N is slightly higher than VIC, during which time the SPLASH W_n is depleted causing moisture-limited E_n^a to occur. Before which, during the winter and early spring, the SPLASH W_n is saturated and E_n^a follows E_n^p .

Figure 4d shows the daily results for a hot arid desert region in southwestern Arizona with a mean annual temperature of
 10 23 °C and annual precipitation of 39 mm. Over the entire year, SPLASH H_N is higher than VIC, with the largest differences occurring during the summer months. The SPLASH and VIC W_n are both consistently low throughout the year. This water limitation is expressed in the low SPLASH E_n^a . During the summer months, SPLASH E_n^p is slightly higher than VIC.

Figure 4e shows the daily results for an equatorial monsoonal region near the southern tip of Florida with a mean annual temperature of 24 °C and annual precipitation of 1500 mm. There is agreement between SPLASH and VIC H_N throughout
 15 the year; however, SPLASH W_n is higher than all three layers of VIC except for a few days following a large rain event in October. During the drier winter, there is a slight moisture limitation shown in the SPLASH E_n^a . Throughout the year, SPLASH E_n^p is slightly higher than VIC.

Figure 4f shows the daily results for a cold arid steppe region in San Luis Potosí, Mexico with a mean annual temperature of 18 °C and annual precipitation of 346 mm. During the winter, SPLASH H_N is slightly higher than VIC. The SPLASH
 20 W_n remains low throughout the year at a level between the first and second layers of VIC. The moisture limitation results in a lower SPLASH E_n^a throughout the year. The SPLASH and VIC E_n^p agree during the year.

Figure 5 shows the SPLASH monthly integrated evapotranspiration results (E_m^p in solid black, E_m^q in dotted black, and E_m^a in dashed red) along with two monthly bioclimatic indices: ΔE_m and α_m . For both the tundra and continental climate sites (Figs. 5a and 5b, respectively), E_m^a is equivalent to E_m^p , which results in constant indices for ΔE_m (i.e., 0 mm) and α_m (i.e.,
 25 1.26). At the annual time scale, ΔE_a and α_a for these two sites are the same as their monthly values and MI is greater than one, suggesting that these are water available sites.

Figure 5c shows the monthly SPLASH results for the temperate with dry summers region. Similar to the daily results (i.e., Fig. 4c), during the dry summer, E_m^a falls below the E_m^p and E_m^q curves. This results in a positive ΔE_m and a drop in α_m during the summer months. At the annual time scale, ΔE_a is 619 mm, which is slightly higher than the annual precipitation
 30 (i.e., 594 mm), and both α_a and MI are less than one (i.e., 0.633 and 0.477, respectively) suggesting that this is a water-limited site.

The hot arid desert region presents a more extreme case as shown in Fig. 5d, where E_m^a is constantly below both E_m^p and E_m^q . This results in a positive bell-shaped ΔE_m curve and a shallow bowl-shaped α_m curve. At the annual time scale, ΔE_a is 1450 mm, which is significantly higher than the annual precipitation (i.e., 39 mm). Also, both α_a and MI are significantly
 35 less than one (i.e., 0.236 and 0.0219, respectively), suggesting that this is a critically water-limited site.

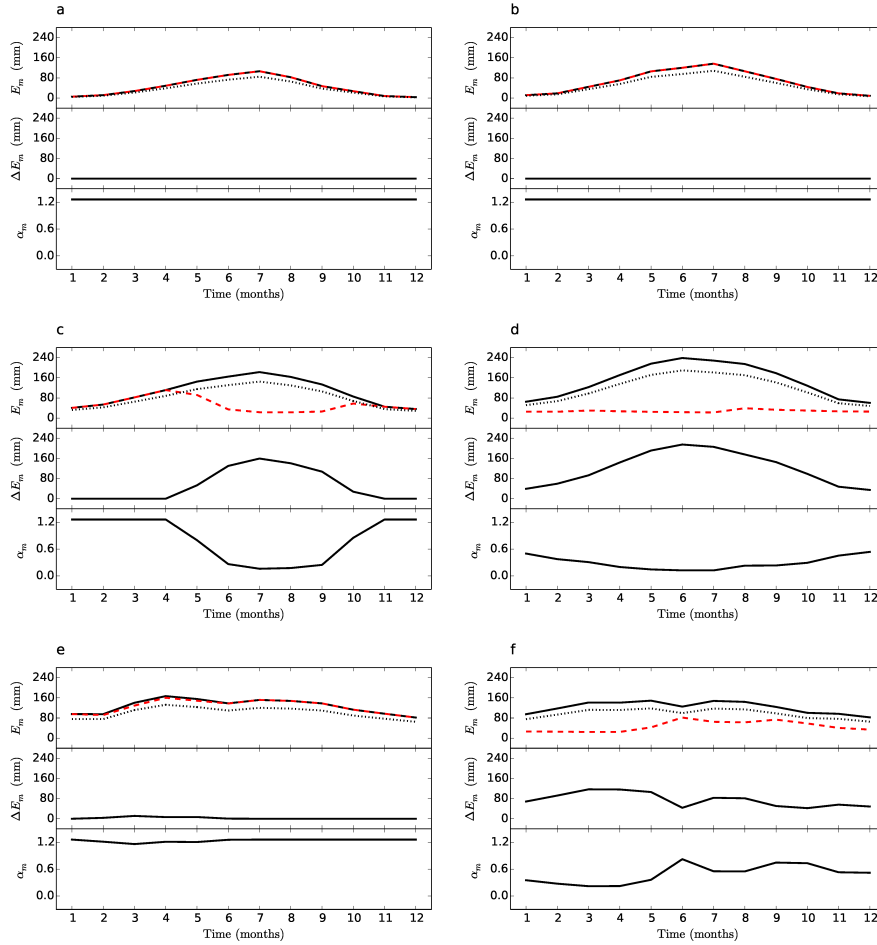


Figure 5. Monthly SPLASH results of evapotranspiration, E_m (potential in solid black, actual in dashed red, and equilibrium in dotted black), climatic water deficit, ΔE_m , and Priestley-Taylor coefficient, α_m for the six climate regions defined in Fig. 3: (a) tundra, (b) continental with warm summers, (c) temperate with dry summers, (d) hot arid desert, (e) equatorial monsoon, and (f) cold arid steppe. Months of the year are represented along the x-axis. Results are of one year (2000 CE).

In contrast at the equatorial monsoonal site, shown in Fig. 5e, E_m^a closely follows the E_m^p curve, which results in a nearly zero ΔE_m and a nearly constant 1.26 α_m . At the annual time scale, ΔE_a is 29 mm, α_a is 1.24, and MI is 0.985, which all suggest that this site is not water limited.

Similar to the hot arid desert, at the high elevation of the cold arid steppe, shown in Fig. 5f, E_m^a is constantly below both E_m^p and E_m^q . Unlike the hot arid desert site, the cold arid steppe site is at a lower latitude, which results in a flatter H_N curve (as shown in Fig. 4f) that leads to a more constant E_m^p curve. At the annual time scale, ΔE_a is 905 mm, which is greater than the annual precipitation (i.e., 346 mm). Both α_a and MI are less than one (i.e., 0.482 and 0.236, respectively), which suggests that this is a water-limited site.

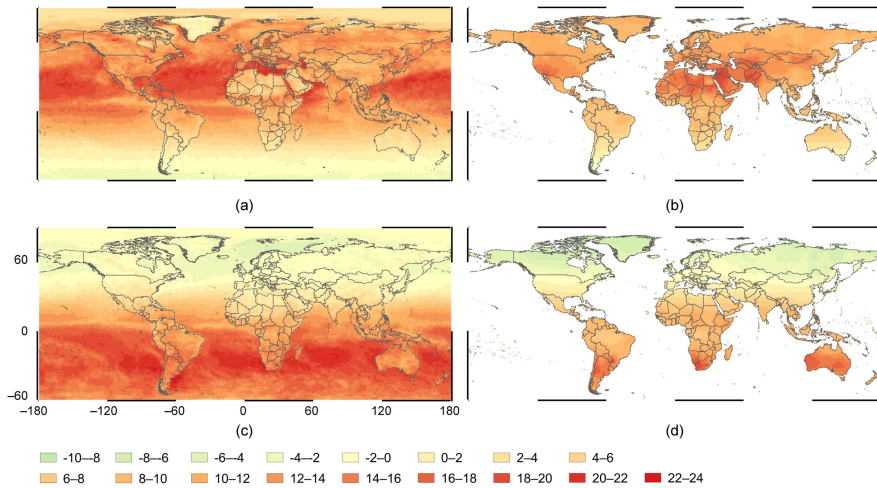


Figure 6. Mean net downward surface radiation flux, MJ m^{-2} , for (a) June 2000 (CERES EBAF); (b) June 2000 (SPLASH); (c) December 2000 (CERES EBAF); December 2000 (SPLASH).

4.2 Global Simulation of Spatial Patterns

For the global simulation, $0.5^\circ \times 0.5^\circ$ CRU TS3.23 data were assembled for one year (2000 CE), including monthly precipitation (mm mo^{-1}), monthly mean daily air temperature ($^\circ\text{C}$), and monthly cloudiness fraction. Monthly precipitation was converted to daily precipitation by dividing the rainfall equally amongst the days in the month. Fractional sunshine hours were calculated based on the one-complement of cloudiness fraction and assumed constant over the month. Mean daily air temperature was also assumed constant over each day of the month. Half-degree land-surface elevation (m above mean sea level) was provided by CRU TS3.22 (Harris et al., 2014). Once again, orbital parameters were assumed constant over the year and calculated for the 2000 CE epoch based on the methods of Berger (1978) and model constants were assigned as per Table 2.

The SPLASH simulations were driven by the data described above, one pixel at a time, starting each pixel with an empty bucket and terminating when a steady-state of soil moisture was reached between the beginning and the end day of the year. Following the spin-up to equilibrate the soil moisture, the model was driven once again to produce daily simulations of net radiation and soil moisture.

Figure 6b and 6d show the SPLASH results of the mean daily net surface radiation flux (MJ m^{-2}) for the months of June and December, respectively. For comparison, the Clouds and the Earth’s Radiant Energy System (CERES) Energy Balanced and Filled (EBAF) average all-sky surface net total flux for June and December 2000 are plotted in Fig. 6a and 6c, respectively. The CERES EBAF net downward radiative flux was converted from W m^{-2} to MJ m^{-2} .

Overall, the SPLASH model produces a reasonable simulation of the latitudinal gradients and seasonal shifts of net surface radiation flux. Locations where the well-watered constant surface albedo assumption fails (e.g., deserts, tundra, and ice sheets),

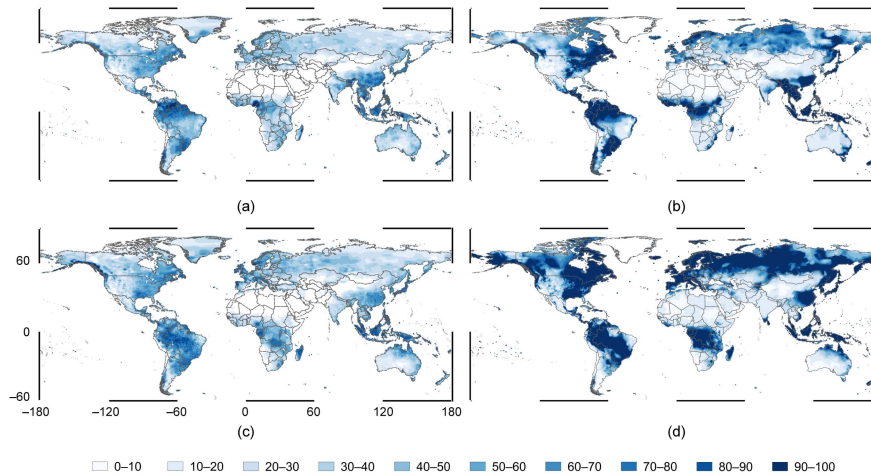


Figure 7. Mean relative soil moisture, %, for (a) June 2000 (NCEP CPC); (b) June 2000 (SPLASH); (c) December 2000 (NCEP CPC); (d) December 2000 (SPLASH). The relative soil moisture is based on the total bucket size (i.e., 760 mm for NCEP CPC and 150 mm for SPLASH).

the SPLASH model simulations are shown to overestimate the CERES EBAF surface radiative flux (especially seen over northern Africa in Fig. 6a and 6b).

Figure 7b and 7d show the SPLASH results of the mean daily relative soil moisture (%) for the months of June and December, respectively. An ice sheet was imposed over Greenland. For comparison, the National Center for Environmental Prediction (NCEP) Climate Prediction Center (CPC) Version 2 mean soil moisture (van den Dool et al., 2003) for June and December 2000 are plotted in Fig. 7a and 7c, respectively. The relative soil moisture in both datasets is computed as the ratio of mm of soil moisture over the total bucket size (i.e., 760 mm in NCEP CPC and 150 mm in SPLASH).

Overall, the SPLASH model simulates soil moisture patterns similar to the NCEP CPC model results. Unlike the NCEP CPC soil moisture, the SPLASH model is shown with a relatively full bucket across wet regions. The lower relative fullness of the NCEP CPC bucket may be contributed to its significantly larger bucket size. Despite the differing magnitudes of soil moisture, the spatial distributions of soil moisture show consistently drier regions in both simulations at both time periods, especially across mid northern latitudes (e.g., eastern North America, northern Africa, and central Asia). Seasonal shifts in soil moisture from June to December are also consistently shown (e.g., southern transition in Africa, eastern transition in South America and northern transition in Australia). There are discrepancies in the spatiotemporal distribution of soil moisture across the high latitude regions (especially Russia). The predominantly saturated conditions in the SPLASH simulations across Russia for December (Fig. 7d) may actually be representative of an increasing snow pack, which could account for these differences.

5 Discussion

The results presented in Sect. 4 are intended to illustrate the dynamic patterns and trends in the SPLASH model outputs across regions and seasons for a single year under steady-state. The SPLASH model results are promising despite the model's simplifications and limited climatic drivers. At the local scale, the comparison between SPLASH and VIC across climate and elevation gradients (i.e., Fig. 4) shows relatively good agreement for E_n^p . There are some discrepancies between H_N , especially at the high-latitude, high-elevation tundra site (i.e., Fig. 4a) and at the low-elevation hot arid desert site (i.e., Fig. 4d), where the SPLASH simulations were higher than VIC for portions to all of the year. These discrepancies are likely due to local deviations from the globally averaged surface albedo. This is especially true when there is snow cover, as SPLASH does not model snowpack. Soil moisture also showed relatively good agreement, except at the equatorial monsoonal site (i.e., Fig. 4e), where the SPLASH simulation was consistently higher than VIC. This discrepancy may be due to the assumed constant maximum soil moisture holding capacity. Furthermore, at the global scale, the SPLASH model reasonably captures the latitudinal gradation of net surface radiation flux (where surface emission assumptions are valid) compared to the CERES EBAF results (i.e., Fig. 6) and produces similar spatial patterns of soil moisture, albeit at different magnitudes, compared to the NCEP CPC soil moisture results (i.e., Fig. 7).

While the methodology presented in Sect. 2 makes numerous assumptions and simplifications (e.g., saturation-excess runoff generation, invariant soil properties, and constant global parameterization), it provides a simple and robust framework for the estimation of radiation components, evapotranspiration, and plant-available moisture requiring only standard meteorological measurements as input. The SPLASH model currently only produces saturation excess runoff. For more realistic runoff generation, other water balance models allow runoff to occur when the bucket is less than full, for example the empirical relationship of runoff to the weighted relative soil moisture in the simple water balance model (Orth et al., 2013). Regarding the bucket size, in principle, W_m in Eq. 21 could be formulated as a property of soil type (as was done, for example, in the original BIOME model), there are some objections to doing so. While W_m has a standard definition in agronomy (i.e., the difference between field capacity and wilting point), the wilting point in reality depends on plant properties. Also, the effective 'bucket size' depends on rooting behavior, which is highly adaptable to the soil wetness profile. The absolute value of daily soil moisture will be influenced by the bucket size (as shown in Fig. 7) and can have an impact on the local hydrology (e.g., Fig. 4e); however, plant-available moisture indexes, such as α (i.e., the ratio of supply-limited to non-supply-limited evapotranspiration), have commonly been found to be relatively insensitive to the bucket size. Regarding localized effects, the standard values presented in Table 2 are representative of reasonable global means; however, it is recommended that local parameterization (e.g., shortwave albedo) be used if and when data are available.

Over the years, a common misconception has developed regarding the calculation of daily actual evapotranspiration (as defined by Federer, 1982), whereby the integration of Eq. 26 is mistakenly interpreted as:

$$E_n^a = \min(S, D), \tag{35}$$

where D (mm d^{-1}) is the total daily demand, given by Eq. 25, and S (mm d^{-1}) is the total daily supply over the hours of positive net radiation, which may be given by:

$$S = \int_{\text{day}} S_w = \int_{-h_n}^{h_n} S_w = \frac{24}{\pi} h_n S_w, \quad (36)$$

where h_n is the net radiation cross-over angle, given by Eq. 15, and the constant coefficient converts the units of radians to hours. As shown in Fig. 2, E_n^a is a piecewise function consisting of two curves overlaid throughout the course of a single day that must be accounted for simultaneously; however, even in some recent model developments, E_n^a is calculated using Eq. 35, including the equilibrium terrestrial biosphere models BIOME3 and BIOME4 (Haxeltine and Prentice, 1996; Kaplan, 2001) and the Lund-Potsdam-Jena Dynamic Global Vegetation Model (Sitch et al., 2003). Only under specific circumstances will Eq. 35 produce correct results. It is the intension of this work to provide a simple analytical solution that correctly accounts for the integration of Eq. 26, which has been provided in the form of Eq. 27b.

Code Availability

The code, in four programming languages (C++, FORTRAN, Python, and R), is available on an online repository under the GNU Lesser General Public License (<https://bitbucket.org/labprentice/splash>). The repository includes the present release (v1.0) and working development of the code (with Makefiles where appropriate), example data, and the user manual. All four versions of the code underwent and passed a set of consistency checks to ensure similar results were produced under the same input conditions. The following describes the requirements for compiling and executing SPLASH v.1.0.

For the C++ version, the code was successfully compiled and executed using the GNU C++ compiler (g++ v.4.8.2) provided by the GNU Compiler Collection (Free Software Foundation, Inc., 2016). It utilizes the C numerics library (cmath), input/output operations library (cstdio), and the standard general utilities library (cstdlib) and references the vector container and string type.

For the FORTRAN version, the code was successfully compiled and executed using the PGI Fortran compiler (pgf95 v.16.1-0) provided by The Portland Group - PGI Compilers and Groups (NVIDIA Corporation, 2016) and the GNU Fortran compiler (gfortran v.4.8.4) provided by the GNU Compiler Collection (Free Software Foundation, Inc., 2016).

For the Python version, the code was successfully compiled and executed using Python 2.7 and Python 3.5 interpreters (Python Software Foundation, 2016). It requires the installation of third-party packages, including NumPy (v.1.10.4 by NumPy Developers, 2016) and SciPy (v.0.17.0 by SciPy Developers, 2016) and utilizes the basic date and time types (datetime), logging facility (logging), Unix-style pathname pattern extension (glob), and miscellaneous operating system interfaces (os) modules.

For the R version, the code was successfully compiled and executed using R-3.2.3 “Wooden Christmas-Tree” (The R Foundation for Statistical Computing, 2015).

Appendix A: Calculating True Longitude

Berger (1978) presents a method for estimating true longitude, λ , for a given day of the year, n , that associates uniform time (i.e., a mean planetary orbit and constant day of the vernal equinox) to Earth's angular position. The formula is based on classical astronomy and is suitable for calculations in palaeoclimatology. The algorithm begins with the calculation of the mean longitude of the vernal equinox, λ_{m0} (rad), assumed to fall on 21 March:

$$\lambda_{m0} = 2 \left[\left(\frac{1}{2} e + \frac{1}{8} e^3 \right) (1 + \beta) \sin \tilde{\omega} - \frac{1}{4} e^2 \left(\frac{1}{2} + \beta \right) \sin 2\tilde{\omega} + \frac{1}{8} e^3 \left(\frac{1}{3} + \beta \right) \sin 3\tilde{\omega} \right], \quad (\text{A1})$$

where $\beta = \sqrt{1 - e^2}$. The mean longitude, λ_m (rad), is then calculated for a given day based on a daily increment with respect to the day of the vernal equinox (i.e., day 80):

$$\lambda_m = \lambda_{m0} + 2\pi(n - 80)N_a^{-1}, \quad (\text{A2})$$

where N_a is total number of days in the year. The mean anomaly, ν_m (rad), is calculated based on the equality presented in Eq. 6:

$$\nu_m = \lambda_m - \tilde{\omega}, \quad (\text{A3})$$

which is then used to determine the true anomaly by:

$$\nu = \nu_m + \left(2e - \frac{1}{4} e^3 \right) \sin \nu_m + \frac{5}{4} e^2 \sin 2\nu_m + \frac{13}{12} e^3 \sin 3\nu_m, \quad (\text{A4})$$

and is converted back to true longitude by:

$$\lambda = \nu + \tilde{\omega}. \quad (\text{A5})$$

The resulting λ should be constrained to an angle within a single orbit (i.e., $0 \leq \lambda \leq 2\pi$).

Appendix B: Calculating Temperature and Pressure Dependencies

The four variables used to calculate the water-to-energy conversion factor, E_{con} , given in Eq. 19 have temperature and/or pressure dependencies that may be solved using the equations presented here.

The temperature-dependent equation for the slope of the saturation vapor pressure-temperature curve, s , can be expressed as (Allen et al., 1998):

$$s = \frac{2.503 \times 10^6 \exp\left(\frac{17.27 T_{air}}{T_{air} + 237.3}\right)}{(T_{air} + 237.3)^2}, \quad (\text{B1})$$

where s ranges from about 11 to 393 Pa K⁻¹ for T_{air} between -20 and 40 °C. Please be aware of the typographical error in this formula as presented in Eq. 7 of Gallego-Sala et al. (2010) where 237.3 is misrepresented as 273.3.

The temperature-dependent equation for the latent heat of vaporization, L_v , may be expressed as (Henderson-Sellers, 1984):

$$L_v = 1.91846 \times 10^6 \left[\frac{T_{air} + 273.15}{(T_{air} + 273.15) - 33.91} \right]^2, \quad (B2)$$

where L_v ranges from about 2.558×10^6 to 2.413×10^6 J K⁻¹ for T_{air} between -20 and 40 °C.

The temperature and pressure dependence of the density of water, ρ_w , may be expressed as (Chen et al., 1977):

$$5 \quad \rho_w = \rho_o \frac{K_o + C_A P_{atm}^* + C_B P_{atm}^{*2}}{K_o + C_A P_{atm}^* + C_B P_{atm}^{*2} - P_{atm}^*}, \quad (B3)$$

where ρ_o (kg m⁻³) is the density of water at 1 atm, K_o (bar) is the bulk modulus of water at 1 atm, C_A (unitless) and C_B (bar⁻¹) are temperature-dependent coefficients, and P_{atm}^* (bar) is the atmospheric pressure (i.e., 1 Pa = 1×10^{-5} bar).

The equation for ρ_o is based on the work of Kell (1975):

$$\rho_o = \sum_{i=0}^8 C_i T_{air}^i. \quad (B4)$$

10 The equation for K_o is also based on the work of Kell (1975):

$$K_o = \sum_{i=0}^5 C_i T_{air}^i. \quad (B5)$$

The equations for C_A and C_B are given as (Chen et al., 1977):

$$C_A = \sum_{i=0}^4 C_i T_{air}^i, \quad (B6)$$

$$15 \quad C_B = \sum_{i=0}^4 C_i T_{air}^i. \quad (B7)$$

The coefficients for T_{air} in Eqns. B4 through B7 are given in Table 3.

The temperature and pressure dependence of the psychrometric constant, γ , may be expressed as (Allen et al., 1998):

$$\gamma = \frac{C_p M_a P_{atm}}{M_v L_v}, \quad (B8)$$

20 where C_p (J kg⁻¹ K⁻¹) is the temperature-dependent specific heat capacity of humid air; M_a (kg mol⁻¹) and M_v (kg mol⁻¹) are the molecular weights of dry air and water vapor, respectively; L_v (J kg⁻¹) is the latent heat of vaporization of water; and P_{atm} (Pa) is the atmospheric pressure. Constants for M_a and M_v are given in Table 2. The temperature dependence of C_p may be assumed negligible (e.g., $C_p = 1.013 \times 10^3$ J kg⁻¹ K⁻¹) or calculated by (Tsilingiris, 2008):

$$C_p = \sum_{i=0}^5 C_i T_{air}^i, \quad (B9)$$

for T_{air} between 0–100 °C. The coefficients of T_{air} are given in Table 3.

Author contributions. I. C. Prentice, M. T. Sykes, and W. Cramer developed the original model theory and methods. A. V. Gallego-Sala, B. J. Evans, H. Wang, and T. W. Davis contributed to model improvements. R. T. Thomas, R. J. Whitley, B. D. Stocker, and T. W. Davis transcribed the new model code and ran simulations. The manuscript was prepared with contributions from all authors.

Acknowledgements. This work was primarily funded by Imperial College London as a part of the AXA Chair Programme on Biosphere and Climate Impacts. It is a contribution to the Imperial College initiative on Grand Challenges in Ecosystems and the Environment, and the ecosystem Modelling and Scaling infrasTructure (eMAST) facility of the Australian Terrestrial Ecosystem Research Network (TERN). TERN is supported by the Australian Government through the National Collaborative Research Infrastructure Strategy (NCRIS). BDS funded by the Swiss National Science Foundation (SNF) and the European Commission's 7th Framework Programme, under Grant Agreement number 282672, EMBRACE project. WC contributes to the Labex OT-Med (n° ANR-11-LABX-0061) funded by the French government through the A*MIDEX project (n° ANR-11-IDEX-0001-02). AGS has been supported by a Natural Environment Research Council grant (NERC grant number NE/I012915/1). VIC simulations utilized the Janus supercomputer, which is supported by the National Science Foundation (award number CNS-0821794) and the University of Colorado Boulder. The Janus supercomputer is a joint effort of the University of Colorado Boulder, the University of Colorado Denver and the National Center for Atmospheric Research. CERES EBAF data were obtained from the NASA Langley Research Center Atmospheric Science Data Center. CPC Soil Moisture data provided by the NOAA/OAR/ESRL PSD, Boulder, Colorado, USA, from their website at <http://www.esrl.noaa.gov/psd/>.

References

- Allen, C. W.: *Astrophysical Quantities*, The Athlone Press, London, 3rd edn., 1973.
- Allen, R. G.: Assessing integrity of weather data for reference evapotranspiration estimation, *J. Irrig. Drain. Div.*, 122, 97–106, 1996.
- Allen, R. G., Pereira, L. S., Raes, D., and Smith, M.: *FAO Irrigation and Drainage Paper No. 56*, Tech. rep., Food and Agriculture Organization of the United Nations, Rome, Italy, 1998.
- Berberan-Santos, M. N., Bodunov, E. N., and Pogliani, L.: On the barometric formula, *Am. J. Phys.*, 65, 404–412, 1997.
- Berger, A. L.: Long-term variations of daily insolation and quaternary climatic changes, *J. Atmos. Sci.*, 35, 2362–2367, 1978.
- Berger, A. L. and Loutre, M. F.: Insolation values for the climate of the last 10 million years, *Quat. Sci. Rev.*, 10, 297–317, 1991.
- Berger, A. L., Loutre, M. F., and Tricot, C.: Insolation and earth's orbital periods, *J. Geophys. Res.*, 98, 10 341–10 362, 1993.
- Budyko, M. I.: The heat balance of the earth's surface, *Sov. Geogr.*, 2, 3–13, 1961.
- Chen, C.-T., Fine, R. A., and Millero, F. J.: The equation of state of pure water determined from sound speeds, *J. Chem. Phys.*, 66, 2142–2144, 1977.
- Cooper, P. I.: The absorption of radiation in solar stills, *Sol. Energy*, 12, 333–346, 1969.
- Cramer, W. and Prentice, I. C.: Simulation of regional soil moisture deficits on a European scale, *Norsk geogr. Tidsskr. – Norwegian J. Geogr.*, 42, 149–151, 1988.
- Cramer, W., Bondeau, A., Woodward, F. I., Prentice, I. C., Betts, R. A., Brovkin, V., Cox, P. M., Fisher, V., Foley, J. A., Friend, A. D., Kucharik, C., Lomas, M. R., Ramankutty, N., Sitch, S., Smith, B., White, A., and Young-Molling, C.: Global response of terrestrial ecosystem structure and function to CO₂ and climate change: results from six dynamic global vegetation models, *Glob. Change Biol.*, 7, 357–373, doi:10.1046/j.1365-2486.2001.00383.x, 2001.
- Dewitte, S., Crommelynck, D., Mekaoui, S., and Joukoff, A.: Measurement and uncertainty of the long-term total solar irradiance trend, *Sol. Phys.*, 224, 209–216, 2004.
- Doorenbos, J. and Pruitt, W. O.: *FAO Irrigation and Drainage Paper No. 24*, Tech. rep., Food and Agriculture Organization of the United Nations, Rome, Italy, 1977.
- Duffie, J. A. and Beckman, W. A.: *Solar engineering of thermal processes*, John Wiley and Sons, New Jersey, 4th edn., 2013.
- Federer, C. A.: Spatial variation of net radiation, albedo and surface temperature of forests, *J. Appl. Meteorol.*, 7, 789–795, 1968.
- Federer, C. A.: Transpirational supply and demand: plant, soil, and atmospheric effects evaluated by simulation, *Water Resour. Res.*, 18, 355–362, 1982.
- Fisher, J. B., Huntzinger, D. N., Schwalm, C. R., and Sitch, S.: Modeling the terrestrial biosphere, *Annu. Rev. Env. Resour.*, 39, 91–123, doi:10.1146/annurev-environ-012913-093456, 2014.
- Fröhlich, C.: Solar irradiance variability since 1978: Revision of the PMOD composite during solar cycle 21, *Space Sci. Rev.*, 125, 53–65, 2006.
- Gallego-Sala, A. V. and Prentice, I. C.: Blanket peat biome endangered by climate change, *Nat. Clim. Ch.*, 3, 152–155, doi:10.1038/nclimate1672, 2012.
- Gallego-Sala, A. V., Clark, J. M., House, J. I., Orr, H. G., Prentice, I. C., Smith, P., Farewell, T., and Chapman, S. J.: Bioclimatic envelope model of climate change impacts on blanket peatland distribution in Great Britain, *Clim. Res.*, 45, 151–162, doi:10.3354/cr00911, 2010.
- Ge, S., Smith, R. G., Jacovides, C. P., Kramer, M. G., and Carruthers, R. I.: Dynamics of photosynthetic flux density (PPFD) and estimates in coastal northern California, *Theor. Appl. Climatol.*, 105, 107–118, doi:10.1007/s00704-010-0368-6, 2011.

- Harris, I., Jones, P. D., Osborn, T. J., and Lister, D. H.: Updated high-resolution grids of monthly climatic observations - the CRU TS3.10 Dataset, *Int. J. Climatol.*, 34, 623–642, doi:10.1002/joc.3711, 2014.
- Harrison, S. P., Prentice, I. C., Barboni, D., Kohfeld, K. E., Ni, J., and Sutra, J.-P.: Ecophysiological and bioclimatic foundations for a global plant functional classification, *J. Veg. Sci.*, 21, 300–317, doi:10.1111/j.1654-1103.2009.01144.x, 2010.
- 5 Haxeltine, A. and Prentice, I. C.: BIOME3: An equilibrium terrestrial biosphere model based on ecophysiological constraints, resource availability, and competition among plant functional types, *Global Biogeochem. Cycles*, 10, 693–709, 1996.
- Henderson-Sellers, B.: A new formula for latent heat of vaporization of water as a function of temperature, *Q. J. R. Meteorol. Soc.*, 110, 1186–1190, 1984.
- Hulme, D., Conway, D., Jones, P. D., Jiang, T., Barrow, E. M., and Turney, C.: Construction of a 1961–1990 European climatology for
10 climate change modelling and impact applications, *Int. J. Climatol.*, 15, 1333–1363, 1995.
- Kaplan, J. O.: Geophysical Applications of Vegetation Modeling, Ph.D. thesis, Lund University, Lund, 2001.
- Kell, G. S.: Density, thermal expansivity, and compressibility of liquid water from 0° to 150°C: Correlations and tables for atmospheric pressure and saturation reviewed and expressed on 1968 temperature scale, *J. Chem. Eng. Data*, 20, 97–105, 1975.
- Knorr, W. and Heimann, M.: Impact of drought stress and other factors on seasonal land biosphere CO₂ exchange studied through an
15 atmospheric tracer transport model, *Tellus*, 47B, 471–489, 1995.
- Kopp, G. and Lean, J. L.: A new, lower value of total solar irradiance: Evidence and climate significance, *Geophys. Res. Lett.*, 38, doi:10.1029/2010GL045777, 2011.
- Kottek, M., Grieser, J., Beck, C., Rudolf, B., and Rubel, F.: World map of the Köppen-Geiger climate classification updated, *Meteorol. Z.*, 15, 259–263, doi:10.1127/0941-2948/2006/0130, 2006.
- 20 Lhomme, J.-P.: A theoretical basis for the Priestley-Taylor coefficient, *Bound.-Lay. Meteorol.*, 82, 179–191, 1997.
- Linacre, E. T.: Further studies of the heat transfer from a leaf, *Plant Physiol.*, 42, 651–658, 1967.
- Linacre, E. T.: Estimating the net-radiation flux, *Agr. Meteorol.*, 5, 49–63, 1968.
- Livneh, B., Bohn, T. J., Pierce, D. W., Munoz-Arriola, F., Nijssen, B., Vose, R., Cayan, D. R., and Brekke, L.: A spatially comprehensive, hydrometeorological data set for Mexico, the U.S., and Southern Canada 1950–2013, *Sci. Data*, 2, 1–12, doi:10.1038/sdata.2015.42, 2015.
- 25 McCree, K. J.: Test of current definitions of photosynthetically active radiation against leaf photosynthesis data, *Agr. Meteorol.*, 10, 443–453, 1972.
- Meek, D. W., Hatfield, J. L., Howell, T. A., Idso, S. B., and Reginato, R. J.: A generalized relationship between photosynthetically active radiation and solar radiation, *Agron. J.*, 76, 939–945, 1984.
- Meng, T.-T., Wang, H., Harrison, S. P., Prentice, I. C., Ni, J., and Wang, G.: Responses of leaf traits to climatic gradients: adaptive variation
30 versus compositional shifts, *Biogeosciences*, 12, 5339–5352, doi:10.5194/bg-12-5339-2015, 2015.
- Middleton, N. and Thomas, D., eds.: *World Atlas of Desertification*, John Wiley and Sons, Inc., New York, 2nd edn., 1997.
- Moldover, M. R., Trusler, J. P. M., Edwards, T. J., Mehl, J. B., and Davis, R. S.: Measurement of the universal gas constant R using a spherical acoustic resonator, *J. Res. Natl. Bur. Stand.*, 93, 85–144, 1988.
- Monteith, J. L.: *Symposia of the Society for Experimental Biology*, vol. 19, chap. Evaporation and environment, pp. 205–234, Academic
35 Press, Inc., New York, 1965.
- Monteith, J. L. and Unsworth, M. H.: *Principles of Environmental Physics*, Butterworth-Heinemann, Oxford, 2nd edn., 1990.
- New, M., Hulme, M., and Jones, P.: Representing twentieth-century space-time climate variability. Part I: Development of a 1961–90 mean monthly terrestrial climatology, *J. Clim.*, 12, 829–856, 1999.

- Orth, R., Koster, R. D., and Seneviratne, S. I.: Inferring soil moisture memory from streamflow observations using a simple water balance model, *J. Hydrometeorol.*, 14, 1773–1790, doi:10.1175/JHM-D-12-099.1, 2013.
- Penman, H. L.: Natural evaporation from open water, bare soil and grass, *Proc. R. Soc. Lond. A*, 193, 120–145, doi:10.1098/rspa.1948.0037, 1948.
- 5 Prentice, I. C. and Cowling: *Encyclopedia of Biodiversity*, chap. Dynamic global vegetation models, pp. 607–689, Academic Press, Inc., Waltham, 2nd edn., 2013.
- Prentice, I. C., Cramer, W., Harrison, S. P., Leemans, R., Monserud, R. A., and Solomon, A. M.: A global biome model based on plant physiology and dominance, soil properties and climate, *J. Biogeogr.*, 19, 117–134, 1992.
- Prentice, I. C., Sykes, M. T., and Cramer, W.: A simulation model for the transient effects of climate change on forest landscapes, *Ecol. Modell.*, 65, 51–70, 1993.
- 10 Prentice, I. C., Liang, X., Medlyn, B. E., and Wang, Y.-P.: Reliable, robust and realistic: the three R's of next-generation land-surface modelling, *Atmos. Chem. Phys. Discuss.*, 14, 24 811–24 861, doi:10.5194/acpd-14-24811-2014, 2014.
- Priestley, C. H. B. and Taylor, R. J.: On the assessment of surface heat flux and evaporation using large-scale parameters, *Mon. Weather Rev.*, 100, 81–92, 1972.
- 15 Quillet, A., Peng, C., and Garneau, M.: Toward dynamic global vegetation models for simulating vegetation-climate interactions and feedbacks: recent developments, limitations, and future challenges, *Environ. Rev.*, 18, 333–353, doi:10.1139/A10-016, 2010.
- Raupach, M. R.: Equilibrium evaporation and the convective boundary layer, *Bound.-Lay. Meteorol.*, 96, 107–141, 2000.
- Raupach, M. R.: Combination theory and equilibrium evaporation, *Q.J.R. Meteorol. Soc.*, 127, 1149–1181, doi:10.1002/qj.49712757402, 2001.
- 20 Sellers, P. J.: Canopy reflectance, photosynthesis and transpiration, *Int. J. Remote Sens.*, 6, 1335–1372, doi:10.1080/01431168508948283, 1985.
- Sitch, S., Smith, B., Prentice, I. C., Arneth, A., Bondeau, A., Cramer, W., Kaplan, J. O., Levis, S., Lucht, W., Sykes, M. T., Thonicke, K., and Venevsky, S.: Evaluation of ecosystem dynamics, plant geography and terrestrial carbon cycling in the LPJ dynamic global vegetation model, *Glob. Change Biol.*, 9, 161–185, doi:10.1046/j.1365-2486.2003.00569.x, 2003.
- 25 Spencer, J. W.: Fourier series representation of the position of the sun, *Search*, 2, 172, 1971.
- Stanhill, G. and Fuchs, M.: The relative flux density of photosynthetically active radiation, *J. Appl. Ecol.*, 14, 317–322, 1977.
- Stephenson, N. L.: Actual evapotranspiration and deficit: biologically meaningful correlates of vegetation distribution across spatial scales, *J. Biogeogr.*, 25, 855–870, 1998.
- Swift, Jr., L. W.: Algorithm for solar radiation on mountain slopes, *Water Resour. Res.*, 12, 108–112, 1976.
- 30 Sykes, M. T. and Prentice, I. C.: Boreal forest futures: modelling the controls on tree species range limits and transient responses to climate change, *Water, Air, Soil Pollut.*, 82, 415–428, 1995.
- Sykes, M. T. and Prentice, I. C.: Climate change, tree species distributions and forest dynamics: a case study in the mixed conifer/northern hardwoods zone of Northern Europe, *Clim. Change*, 34, 161–177, 1996.
- Sykes, M. T., Prentice, I. C., and Cramer, W.: A bioclimatic model for the potential distributions of north European tree species under present and future climates, *J. Biogeogr.*, 23, 203–233, 1996.
- 35 Thekaekara, M. P. and Drummond, A. J.: Standard values for the solar constant and its spectral components, *Nature, Phys. Sci.*, 229, 6–9, 1971.
- Thornthwaite, C. W.: An approach toward a rational classification of climate, *Geogr. Rev.*, 38, 55–94, 1948.

- Tsilingiris, P. T.: Thermophysical and transport properties of humid air at temperature range between 0 and 100 °C, *Energy Convers. Manage.*, 49, 1098–1110, 2008.
- Ukkola, A. M., Prentice, I. C., Keenan, T. F., van Dijk, A. I. J. M., Viney, N. R., Myneni, R. B., and Bi, J.: Reduced streamflow in water-stressed climates consistent with CO₂ effects on vegetation, *Nat. Clim. Change*, doi:10.1038/nclimate2831, 2015.
- 5 van den Dool, H., Huang, J., and Fan, Y.: Performance and analysis of the constructed analogue method applied to U.S. soil moisture over 1981–2001, *J. Geophys. Res.*, 108, 1–16, doi:10.1029/2002JD003114, 2003.
- Wang, H., Prentice, I. C., and Davis, T. W.: Biophysical constraints on gross primary production by the terrestrial biosphere, *Biogeosciences*, 11, 5987–6001, doi:10.5194/bg-11-5987-2014, 2014.
- Weedon, G. P., Balsamo, G., Bellouin, N., Gomes, S., Best, M. J., and Viterbo, P.: The WFDEI meteorological forcing data set: WATCH
10 Forcing Data methodology applied to ERA-Interim reanalysis data, *Water Resour. Res.*, 50, 7505–7514, doi:10.1002/2014WR015638, 2014.
- Willson, R. C.: Total solar irradiance trend during solar cycles 21 and 22, *Science*, 277, 1963–1965, 1997.
- Woodward, F. I. and Lomas, M. R.: Vegetation dynamics—simulating responses to climatic change, *Biol. Rev.*, 79, 643–670, doi:10.1017/S1464793103006419, 2004.
- 15 Woolf, H. M.: On the computation of solar elevation angles and the determination of sunrise and sunset times, Tech. Rep. NASA-TM-X-164, National Aeronautics and Space Administration, Washington, DC, 1968.

Table 1. Nomenclature.

Instantaneous	
S_w	evaporative supply rate, mm h^{-1}
D_p	evaporative demand rate, mm h^{-1}
E^q	equilibrium evapotranspiration rate, mm h^{-1}
E^p	potential evapotranspiration rate, mm h^{-1}
E^a	actual evapotranspiration rate, mm h^{-1}
I_o	extraterrestrial solar radiation flux, W m^{-2}
I_N	net radiation flux, W m^{-2}
I_{SW}	net shortwave solar radiation flux, W m^{-2}
I_{LW}	net longwave radiation flux, W m^{-2}
Daily	
W_n	soil moisture, mm
P_n	precipitation, mm d^{-1}
C_n	condensation, mm d^{-1}
RO	runoff, mm
E_n^q	equilibrium evapotranspiration, mm d^{-1}
E_n^p	potential evapotranspiration, mm d^{-1}
E_n^a	actual evapotranspiration, mm d^{-1}
H_o	solar irradiation, $\text{J m}^{-2} \text{d}^{-1}$
H_N	net surface radiation, $\text{J m}^{-2} \text{d}^{-1}$
H_N^+	positive net surface radiation, $\text{J m}^{-2} \text{d}^{-1}$
H_N^-	negative net surface radiation, $\text{J m}^{-2} \text{d}^{-1}$
Q_n	photosynthetically active radiation, $\text{mol m}^{-2} \text{d}^{-1}$
S_f	fraction of bright sunshine hours, unitless
T_{air}	mean air temperature, $^{\circ}\text{C}$
Monthly	
E_m^q	equilibrium evapotranspiration, mm mo^{-1}
E_m^p	potential evapotranspiration, mm mo^{-1}
E_m^a	actual evapotranspiration, mm mo^{-1}
ΔE_m	climatic water deficit, mm mo^{-1}
α_m	Priestley-Taylor coefficient, unitless

Table 1 (continued). Nomenclature.

Miscellaneous	
$\cos \theta_z$	inclination factor, unitless
δ	declination angle, rad
d_r	distance factor, unitless
ε	obliquity, rad
e	eccentricity, unitless
E_{con}	water to energy conversion factor, $\text{m}^3 \text{J}^{-1}$
γ	psychrometric constant, Pa K^{-1}
h	hour angle, rad
h_i	intersection of evaporative rates hour angle, rad
h_n	net radiation crossover hour angle, rad
h_s	sunset hour angle, rad
i	day of month (1–31)
λ	true longitude, rad
L_v	latent heat of vaporization of water, J kg^{-1}
ν	true anomaly, rad
n	day of year (i.e., 1–365)
N_a	total number of days in a year (e.g., 365)
N_m	total number of days in a given month (e.g., 31)
$\tilde{\omega}$	longitude of perihelion, rad
ϕ	latitude, rad
P_{atm}	atmospheric pressure, Pa
ρ_w	density of water, kg m^{-3}
r_u	$\sin \delta \sin \phi$, unitless
r_v	$\cos \delta \cos \phi$, unitless
r_w	$(1 - \beta_{sw}) \tau I_{sc} d_r$, W m^{-2}
r_x	$3.6 \times 10^6 (1 + \omega) E_{con}$, $\text{mm m}^2 \text{W}^{-1} \text{h}^{-1}$
s	slope of saturated vapor pressure-temperature curve, Pa K^{-1}
τ	transmittivity, unitless
τ_o	transmittivity at mean sea level, unitless
z	elevation above mean sea level, m

Table 2. Constants and Standard Values.

Variable	Units	Description
A	107 °C	empirical constant, Eq. 13 (Monteith and Unsworth, 1990)
β_{sw}	0.17	shortwave albedo, Eq. 10 (Federer, 1968)
β_{vis}	0.03	visible light albedo, Eq. 17 (Sellers, 1985)
b	0.20	empirical constant, Eq. 13 (Linacre, 1968)
c	0.25	cloudy transmittivity, Eq. 12 (Linacre, 1968)
d	0.50	angular coefficient of transmittivity, Eq. 12 (Linacre, 1968)
fFEC	2.04 $\mu\text{mol J}^{-1}$	flux-to-energy conversion, Eq. 17 (Meek et al., 1984)
g	9.80665 m s^{-2}	standard gravity, Eq. 20 (Allen, 1973)
I_{sc}	1360.8 W m^{-2}	solar constant, Eq. 2 (Kopp and Lean, 2011)
L	0.0065 K m^{-1}	mean adiabatic lapse rate, Eq. 20 (Allen, 1973)
M_a	0.028963 kg mol^{-1}	molecular weight of dry air, Eq. 20 (Tsilingiris, 2008)
M_v	0.01802 kg mol^{-1}	molecular weight of water vapor, Eq. B8 (Tsilingiris, 2008)
ω	0.26	entrainment factor, Eq. 22 (Priestley and Taylor, 1972)
P_o	101325 Pa	standard sea-level pressure, Eq. 20 (Allen, 1973)
R	8.31447 $\text{J mol}^{-1} \text{K}^{-1}$	universal gas constant, Eq. 20 (Moldover et al., 1988)
S_c	1.05 mm h^{-1}	supply rate constant, Eq. 21 (Federer, 1982)
T_o	288.15 K	base temperature, Eq. 20 (Berberan-Santos et al., 1997)
W_m	150 mm	soil moisture capacity, Eq. 21 (Cramer and Prentice, 1988)

Table 3. Coefficients of T_{air} .

	ρ_o (kg m^{-3}) Eq. B4	K_o (bar) Eq. B5	C_A (unitless) Eq. B6	C_B (bar^{-1}) Eq. B7	C_p ($\text{J kg}^{-1} \text{K}^{-1}$) Eq. B9
C_0	$+9.998395 \times 10^2$	$+1.96520 \times 10^4$	+3.26138	$+7.2061 \times 10^{-5}$	$+1.004571 \times 10^3$
C_1	$+6.78826 \times 10^{-2}$	$+1.48183 \times 10^2$	$+5.223 \times 10^{-4}$	-5.8948×10^{-6}	+2.050633
C_2	-9.08659×10^{-3}	-2.29995	$+1.324 \times 10^{-4}$	$+8.6990 \times 10^{-8}$	-1.631537×10^{-1}
C_3	$+1.02213 \times 10^{-4}$	$+1.28100 \times 10^{-2}$	-7.655×10^{-7}	-1.0100×10^{-9}	$+6.212300 \times 10^{-3}$
C_4	-1.35439×10^{-6}	-4.91564×10^{-5}	$+8.584 \times 10^{-10}$	$+4.3220 \times 10^{-12}$	-8.830479×10^{-5}
C_5	$+1.47115 \times 10^{-8}$	$+1.03553 \times 10^{-7}$	—	—	$+5.071307 \times 10^{-7}$
C_6	-1.11663×10^{-10}	—	—	—	—
C_7	$+5.04407 \times 10^{-13}$	—	—	—	—
C_8	-1.00659×10^{-15}	—	—	—	—